Pose Optimization for Autonomous Driving Datasets using Neural Rendering Models

Quentin Herau^{1,2}, Nathan Piasco¹, Moussab Bennehar¹, Luis Roldão¹, Dzmitry Tsishkou¹, Bingbing Liu¹, Cyrille Migniot³, Pascal Vasseur⁴ and Cédric Demonceaux²

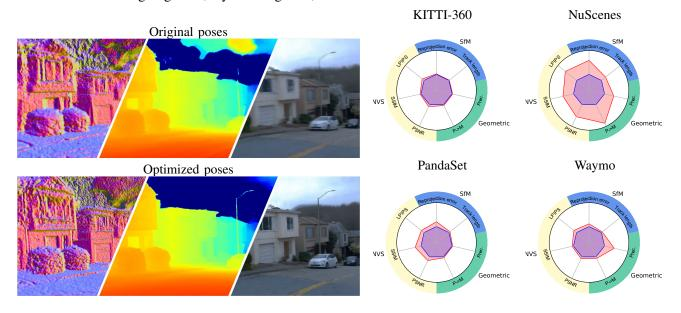


Fig. 1: **Dataset pose improvement:** Left, rendering comparison between original poses and optimized poses on Waymo open dataset [1] (from left to right: normal map, depth map and RGB rendering). Right, the changes in metrics between the original poses (in blue) and the poses optimized with MOISST (in red) for each dataset, grouped in 3 categories: Novel View Synthesis, Structure-from-Motion, Geometric.

Abstract-Autonomous driving systems rely on accurate perception and localization of the ego car to ensure safety and reliability in challenging real-world driving scenarios. Public datasets play a vital role in benchmarking and guiding advancement in research by providing standardized resources for model development and evaluation. However, potential inaccuracies in sensor calibration and vehicle poses within these datasets can lead to erroneous evaluations of downstream tasks, adversely impacting the reliability and performance of the autonomous systems. To address this challenge, we propose a robust optimization method based on Neural Radiance Fields (NeRF) to refine sensor poses and calibration parameters, enhancing the integrity of dataset benchmarks. To validate improvement in accuracy of our optimized poses without ground truth, we present a thorough evaluation process, relying on reprojection metrics, Novel View Synthesis rendering quality, and geometric alignment. We demonstrate that our method achieves significant improvements in sensor pose accuracy. By optimizing these critical parameters, our approach not only improves the utility of existing datasets but also paves the way for more reliable

¹Noah's Ark Lab, Huawei. {Quentin.Herau, Nathan.Piasco, Moussab.Bennehar, Luis.Roldao, Dzmitry.Tsishkou, liu.bingbing}@huawei.com

²ICR UMB CNRS 6303 Université de Bour

²ICB UMR CNRS 6303, Université de Bourgogne, France. {Quentin.Herau@etu., Cedric.Demonceaux@}u-bourgogne.fr

³ImViA UR 7535, Université de Bourgogne, France. Cyrille.Migniot@u-bourgogne.fr

⁴MIS UR 4290, Université de Picardie Jules Verne, France. Pascal.Vasseur@u-picardie.fr autonomous driving models. To foster continued progress in this field, we make the optimized sensor poses publicly available, providing a valuable resource for the research community.

Index Terms—Pose optimization, Neural Radiance Field, 3D Reconstruction, Extrinsic calibration, Trajectory optimization, Multi-modal, Multi-sensor.

I. Introduction

UTONOMOUS driving presents unique challenges that set it apart from other domains. Safety stands as the cornerstone of this field, requiring systems to reliably protect passengers in a wide variety of conditions, including rare and critical edge cases. The complexity of road environments, characterized by dynamic interactions, unpredictable agent behaviors, and diverse environmental conditions, further amplifies the difficulty. Autonomous driving systems must accurately perceive their surroundings, predict the movements of other agents, and make split-second decisions to navigate safely and efficiently.

Publicly available driving datasets [1]–[4] play a pivotal role in addressing these challenges. By providing diverse and reliable data, these datasets enable researchers to train or evaluate their solutions, ensuring that they can generalize across a wide range of scenarios and conditions. Furthermore, public datasets facilitate rigorous testing, helping validate that

autonomous driving systems can handle complex interactions and maintain passenger safety in all circumstances. These datasets are instrumental in refining perception, mapping, and decision-making algorithms, driving innovation, and progress in the field of autonomous driving.

As different methods are improved and refined, the progress becomes more and more incremental ¹. These minor advancements frequently fall within the precision margins of the dataset itself, raising concerns that current methods might be overfitting to the dataset's inaccuracies rather than achieving performance gains. This overfitting suggests that the true potential for algorithmic improvement is hindered by limitations inherent in the datasets, such as pose inaccuracies and calibration errors.

These inaccuracies in sensor poses can lead to a cascading impact on downstream tasks. For instance, models like Neural Radiance Fields (NeRF) [5], which rely heavily on accurate pose data for high-fidelity 3D scene representation and novel view synthesis, can suffer from degraded performance when poses are erroneous. Furthermore, inaccuracies in camera-LiDAR calibration can lead to systematic errors in supervised learning-based calibration methods, as the information used for supervision is incorrect. This misalignment not only affects the performance of developed models but can also compromise the fair and accurate evaluation of different methodologies.

Recently, approaches leveraging NeRF have been developed to enhance geometric and photometric consistency between sensor data (e.g. images, LiDAR scans) and the learned 3D models [6]–[11]. These methods have demonstrated significant improvements in pose estimation and calibration parameter refinement. In this work, we propose a unified solution that simultaneously optimizes poses and refines calibration parameters, building upon the models of MOISST [9] and SOAC [10]. We demonstrate an improvement in accuracy with our optimized poses over the original poses through a comprehensive set of geometric and photometric metrics, demonstrating the effectiveness of the proposed method. In summary, we propose the following contributions in this paper.

- We introduce a robust NeRF-based optimization method capable of refining both sensor poses and calibration parameters, enhancing the precision of publicly available autonomous driving datasets.
- We introduce a comprehensive set of evaluation metrics to demonstrate pose precision, including metrics that assess both visual and geometric accuracy, without relying on provided ground truth poses.

These contributions aim to facilitate more accurate and meaningful research, minimizing errors in model training and evaluation that stem from dataset inaccuracies. Optimized poses and calibration will be made publicly available, enabling the research community to benefit from enhanced data quality for downstream tasks and more reliable evaluations.

II. RELATED WORK

A. Pose estimation

1) Classical methods: classical pose estimation methods based on multiview geometry have laid the groundwork for 3D reconstruction and navigation in computer vision and robotics. Structure-from-Motion (SfM) techniques, such as COLMAP [12], have been widely used to estimate camera poses and 3D scene structure from 2D image sequences by matching features like SIFT [13] and performing bundle adjustment. While effective in controlled environments, SfM can struggle with dynamic scenes and sparse features, leading to inaccuracies.

Visual Odometry (VO) methods estimate the relative motion of a camera by tracking features between sequential frames [14]. Chien et al. [15] benchmarked the performance comparison depending on the feature extractor used. VO can operate in real time but is prone to drift over long sequences due to accumulated errors.

Expanding on VO, Visual Simultaneous Localization and Mapping (V-SLAM) integrates pose estimation with environment mapping, enabling more consistent trajectory estimates [16], [17]. V-SLAM systems use loop closure techniques to mitigate drift, but they often require feature-rich settings and may struggle in dynamic or texture-poor environments.

Despite their strengths, these classical methods often assume static conditions and rely on hand-crafted features, limiting their adaptability in diverse scenarios. These limitations have motivated the development of deep learning and neural rendering approaches, which seek to overcome these challenges by leveraging learned representations for more robust and flexible pose estimation.

As for LiDAR-based odometry, it mostly focuses on accurately aligning 3D point clouds to track movement. The foundational method comes from the least-square fitting of two 3D point sets, which led to the development of the Iterative Closest Point (ICP [18]) algorithm. KISS-ICP [19] revisits ICP, advocating for a simpler and more robust point-to-point registration. Building on these concepts, LOAM [20] introduced a real-time approach to odometry and mapping by decoupling these tasks, while LeGO-LOAM [21] optimized this framework for ground-based vehicles operating in variable terrain. F-LOAM [22] further improved this by focusing on faster processing while maintaining accuracy, making it more practical for real-time applications.

By tightly coupling both LiDAR and camera data, accuracy and robustness in SLAM systems have been significantly improved. V-LOAM [23] pioneered this integration by combining high-frequency visual odometry with LiDAR-based motion refinement to minimize drift. LIMO [24] leveraged LiDAR depth to enhance monocular feature tracking, while CamVox [25] optimized large-scale mapping using Livox LiDAR. TVL-SLAM [26] advanced sensor fusion through tightly coupled backend optimization, and Huang et al. [27] refined feature extraction by incorporating both point and line features. DVL-SLAM [28] introduced an optimized sparse depth-based visual-LiDAR odometry framework, and SDV-LOAM [29] integrated semi-direct visual odometry with Li-DAR scan matching for high-frequency pose estimation. These

¹https://www.cvlibs.net/datasets/kitti/eval_odometry.php

contributions have collectively advanced the state of Camera-LiDAR SLAM, enabling more precise and reliable localization in diverse environments.

2) Deep learning-based methods: Deep learning has significantly advanced pose estimation by overcoming some limitations inherent in traditional methods.

Deep learning-based visual odometry and V-SLAM systems have emerged, blending learned feature extraction with motion estimation. Approaches such as DeepVO [30] employed recurrent neural networks (RNNs) to model temporal dependencies between frames, thus enhancing pose tracking over longer sequences.

Deep learning has also significantly impacted the SfM field, improving key components such as feature detection and matching. SuperPoint [31] introduced self-supervised keypoint detection, enabling more robust and real-time performance. SuperGlue [32] took this further by using a graph neural network (GNN) to improve feature matching and correspondence, especially in challenging environments.

More recently, feedforward SfM methods have emerged, replacing traditional pipelines with end-to-end deep learning frameworks. VGGSfM [33] integrates both visual and geometric principles into a fully differentiable system that optimizes all stages of the SfM process, including point tracking, pose estimation, and 3D reconstruction, yielding state-of-the-art performance. DUST3R [34] employs a transformer-based architecture to perform unsupervised 3D reconstruction, learning dense local features and handling extreme viewpoint changes and occlusions. Building upon this, MAST3R [35] introduces multi-scale attention, further enhancing feature matching and refining 3D scene reconstruction for better robustness and speed.

For LiDAR odometry, deep learning is shifting the approach by learning features directly from raw LiDAR data. Wang et al. [36] demonstrates how deep learning can improve the efficiency and accuracy of odometry by learning compact, discriminative features. DeepVCP [37] integrates deep learning into the ICP framework, enhancing point cloud registration with a data-driven approach. These deep learning methods offer greater adaptability and robustness compared to traditional feature-based techniques, enabling LiDAR odometry to handle more complex and dynamic environments.

As for Visual-LiDAR SLAM leveraging deep-learning techniques, Lvio-Fusion [38] introduces a tightly coupled SLAM framework integrating stereo cameras, LiDAR, IMU, and GPS. It utilizes graph-based optimization and reinforcement learning to adaptively adjust sensor weights, enhancing performance in diverse environments. Meanwhile, Self-VLO [39] proposes a self-supervised learning approach for visual-LiDAR odometry, incorporating a siamese network with a flip consistency loss to enforce structural consistency.

However, while these models demonstrate better generalization and robustness, they typically require substantial amounts of training data and struggle in environments that differ significantly from their training domain.

Despite these challenges, deep learning approaches have opened new pathways for scalable and adaptive pose estimation, particularly when processing large amounts of data with the support of powerful computational resources. This has set the stage for more sophisticated techniques involving learned representations, transitioning into the realm of neural rendering.

3) Neural Rendering-Based Methods: Neural rendering has transformed 3D scene representation and pose optimization by merging neural networks with differentiable rendering techniques. NeRF (Neural Radiance Fields) [5] is a standout method that models 3D scenes as continuous volumetric fields, allowing for high-quality novel view synthesis from sparse input images. By leveraging photometric consistency, NeRF jointly optimizes scene geometry and camera poses, circumventing the limitations of explicit feature matching and proving effective in complex or feature-scarce environments.

Building on this, methods like NeRF⁻⁻ [6] proposes to simultaneously optimize the poses and the NeRF. BARF (Bundle-Adjusting NeRF) [7] incorporate principles of bundle adjustment to enable joint pose refinement and scene reconstruction. The model uses progressive positional encoding to tackle local minima challenges, allowing for pose estimates to be refined throughout the training process. SCNeRF [40] proposes to also optimize the intrisic parameters of the camera, including distorsion. Nope-NeRF [41] relies on depth sequential monocular depth consistency and UP-NeRF [42] on DINO features [43]. Going beyond just optimizing poses, some methods propose to find these poses with NeRF-based SLAM techniques. iMAP [44] was the first real-time SLAM system using a multi-layer perceptron (MLP) as the sole scene representation, demonstrating efficient incremental mapping with a compact neural model. NICE-SLAM [45] extended this concept with a hierarchical feature grid, significantly improving scalability and reconstruction detail in large environments. Orbeez-SLAM [46] introduced NeRF-based mapping integrated with ORB-SLAM2 [47] for more efficient scene adaptation without pre-training. NeRF-SLAM [48] further refined monocular SLAM with hierarchical volumetric neural radiance fields, achieving high-fidelity realtime reconstruction. Recently, PLGSLAM [49] proposed a progressive scene representation with local-to-global bundle adjustment, enhancing robustness and accuracy in large-scale environments.

These methods have demonstrated strong performance in diverse and unstructured environments, surpassing traditional techniques in adaptability and output quality.

For NeRF-based LiDAR odometry, SHINE-Mapping [50] leverages sparse hierarchical NeRF models for large-scale 3D mapping, reducing computational costs while maintaining high-quality reconstructions. NeRF-LOAM [51] integrates these models into the LiDAR odometry process, enabling large-scale incremental updates to the environment, improving both accuracy and efficiency. LONER [52] focuses on real-time SLAM using only LiDAR data and neural representations to maintain map consistency with minimal computational overhead. Similarly, PIN-SLAM [53] uses point-based implicit neural representations to ensure global map consistency, enhancing robustness in dynamic environments. These NeRF-based approaches are pushing the boundaries of LiDAR odometry and SLAM, offering scalable, efficient solutions for large-

scale, real-time applications.

Finally, camera-LiDAR SLAM can also take advantage of implicit neural representations, as proposed by Liu et al. [54] who combine a monocular camera and a lightweight ToF sensor, using neural scene representations for improved pose tracking and dense reconstruction. Rapid-Mapping [55] integrates LiDAR and visual data for real-time dense mapping, preserving high-fidelity textures and achieving efficient large-scale reconstruction.

The use of multiple sensors in these systems has been shown to provide more comprehensive and accurate pose estimations. However, this approach necessitates precise calibration to ensure that data from different sensors align correctly. Calibration remains an essential step to leverage the full potential of multi-sensor input, enhancing the overall robustness and accuracy of pose estimates in complex real-world scenarios.

B. Calibration techniques

Calibration is critical for accurate alignment of data from multiple sensors of different modalities, such as cameras and LiDAR, which is essential for robust 3D perception and mapping. This section outlines the evolution of calibration methods, focusing on target-based, targetless, and neural renderingbased approaches.

- 1) Target-based calibration: Target-based calibration has long been the standard approach for achieving precise alignment between sensors. These methods involve using known calibration patterns, such as checkerboards [56]–[58] or custom fiducial targets [59], [60], to establish the spatial relationships between sensors. Target-based calibration techniques can provide highly accurate results by ensuring that the intrinsic and extrinsic parameters are aligned through controlled experiments. The calibration process typically includes capturing multiple images of the target from different perspectives or having multiple targets, and using algorithms to estimate parameters that minimize reprojection errors. While effective, these methods are limited to controlled environments and often require significant manual effort, making them less suitable for large-scale or real-time applications.
- 2) Targetless calibration: To address the limitations of target-based methods, targetless calibration approaches have been developed, which rely on features naturally present in the environment. These methods use scene elements such as edges [61], [62], planes [63], feature points [64], [65], or mutual information [66], [67] to estimate calibration parameters without the need for specialized targets. For example, algorithms can detect and use prominent lines or surface edges for calibration by leveraging geometric relationships between sensors and the environment. These techniques are advantageous because they can be deployed in varied and unstructured settings, providing more flexibility compared to target-based methods. However, their accuracy may be affected by the quality of the detected features and scene complexity, which can lead to reduced precision in feature-sparse or dynamic environments. Deep learning has further enhanced targetless calibration by training models to predict extrinsic parameters directly from sensor data [68]-[71]. While these

techniques allow online calibration thanks to the low inference speed, they require a well labeled training dataset, and are subject to poor generalization capabilities [10], [72].

3) Neural Rendering-Based calibration: Neural renderingbased calibration methods represent a recent and innovative approach to sensor calibration. These methods leverage the representational power of neural networks combined with differentiable rendering to refine calibration parameters through multi-view photometric consistency. Techniques such as MOISST [9] optimizes calibration by implicitly modeling the 3D scene and sensor relationships, bypassing the need for explicit calibration targets. It can adapt to diverse and challenging environments, continuously refining extrinsic parameters during the training process to maintain alignment. INF [8] first learns the geometry by optimizing LiDAR scan poses, then calibrates a 360° camera by enforcing photometric consistency on the learned geometry. SOAC [10] improves upon the idea by relying on sensor-specific NeRF, taking into account the view overlap between the sensors and enforcing consistency. UniCal [11] relies on keypoint reprojection to improve geometric consistency. 3DGS-Calib [73] combines the speed of Gaussian rasterization with the neural continuous representation for feature learning to allow faster calibration. By aligning sensors through photometric and geometric consistency across views, these methods achieve high accuracy and robustness, making them suitable for complex real-world scenarios, and are used in tasks where precise poses are necessary [74], [75]. The integration of neural rendering in calibration processes allows for the simultaneous optimization of calibration and scene representation, enhancing the overall fidelity of sensor alignment.

C. Pose evaluation without ground truth

From the previous sections, we can deduce that combining calibration and pose optimization can provide robust and accurate results, as each process complements the other. Calibration ensures proper alignment of data from multiple sensors, while pose optimization refines both the trajectory and sensor positions to improve scene reconstruction and navigation coherence. In this work, since the objective is to improve the provided poses, there are no ground truth poses available to assess the accuracy of the obtained poses and calibration.

Pose evaluation in the absence of ground truth remains a critical and unresolved challenge in computer vision, particularly for applications in visual localization and structure-from-motion. Instead of relying on ground truth information, several studies have introduced proxy metrics to assess pose accuracy. For example, COLMAP [12] employs robust feature matching and point triangulation to compute reprojection error, which has become a standard indirect measure of pose quality in incremental SfM pipelines. Complementing this, statistical measures such as the Chi-Square metric [76] quantitatively evaluate the consistency between observed features and the predicted model, while the Mahalanobis distance [77] normalizes these errors by the associated measurement covariances to account for uncertainty. More recent approaches have extended

these ideas by incorporating forward-backward consistency checks over image sequences [78], a strategy that is particularly useful in dynamic and deformable environments. In previous works on pose optimization for novel view synthesis [6], [7], the visual evaluation metrics (PSNR, SSIM, LPIPS) have also been used to evaluate pose accuracy without requiring the ground truth poses [7], [79]. Despite the promise of these metrics and their adoption in evaluation [80], Brachmann et al. [81] have demonstrated that such evaluations tend to favor methods whose underlying assumptions closely mirror those of the reference algorithms, such as SfM or SLAM. This inherent bias underscores the necessity for developing more robust, general-purpose evaluation strategies for camera poses without real ground truth.

In this paper, we integrate a pipeline that combines both calibration and trajectory optimization, enabling consistent updates and reducing the compounded errors that can occur when these processes are handled separately. Leveraging a neural rendering-based framework, we jointly optimize calibration and poses, enhancing both accuracy and stability in complex real-world scenarios. To ensure an unbiased evaluation of our results, we propose a comprehensive assessment using a variety of metrics from different methods. Our experiments demonstrate a consistent improvement over the original poses.

III. METHOD

The goal of this work is twofold: first, to optimize the sensor poses in autonomous driving datasets, and second, to conduct a thorough evaluation using multiple metrics. We introduce a comprehensive approach that simultaneously refines the extrinsic calibration parameters and the vehicle trajectory in a multi-modal, multi-sensor context in section III-A and section III-B, while assessing both through a set of geometric and photometric criteria detailed in section III-C. This framework enables users to select the optimal poses based on the provided metrics.

A. Pipeline

The pipeline consists of all necessary steps to obtain the desired outputs: optimized calibration and trajectory. A visual representation is given in Fig. 2

- Dynamic Filtering: The inclusion of this step depends on whether the optimization model considers dynamic elements. In our work, the models do not handle dynamic objects (vehicles, pedestrians, etc.). However, since most driving datasets provide instance-level bounding boxes, these can be used to filter out such objects. By tracking bounding box motion across frames, dynamic elements are identified. In images, dynamic pixels are removed by reprojecting the boxes on the images, and in LiDAR data, points within these boxes are excluded. As the poses are slightly noisy, enlarged bounding boxes are used to ensure that the dynamic object is fully covered.
- Subsequence Creation: Directly learning from entire driving dataset sequences may pose challenges for NeRF models, as the overall scene size can be too large for

- accurate scene representation. To address this, the sequences are split into smaller subsequences of fixed size. This approach ensures that each NeRF model trained on individual subsequences can maintain a consistent level of detail.
- Extrinsic Calibration Optimization: It is assumed that the transformation between sensors remains static across all sequences, as the sensor setup does not change (unless the car used to capture each sequence is different). To enhance robustness, calibration parameters are optimized across multiple subsequences simultaneously in parallel.
- Trajectory Optimization: After the calibration parameters are fixed for a given dataset, they are reused across all subsequent subsequences. This allows the optimization process to focus solely on refining the trajectory, without altering the calibration.
- Evaluation and Selection: Once the optimized poses are obtained through the refined trajectory and calibration parameters, their accuracy and quality are evaluated through a series of tasks, including keypoint reprojection, geometric consistency, and novel view synthesis. These tasks serve to verify the accuracy of the optimized poses relative to the original ones and assess their robustness across various scenarios. This evaluation process not only identifies potential improvements in pose estimation but also offers a framework for selecting the most accurate set of poses. Additionally, it aids in choosing the most suitable model for the optimization, ensuring the best possible outcomes in both pose accuracy and overall system performance.

B. Optimization process

1) Model: In the pipeline, the calibration and trajectory optimization steps are compatible with any method capable of providing multi-modal, multi-sensor calibration and trajectory optimization. In this paper, we rely on these following models for the optimization with adaptations to align them with the specific requirements of this task:

- MOISST [9]: The principle of this model builds upon the idea from BARF [7]. During optimization of the implicit neural representation, gradients are backpropagated to the input poses of the frames. However, by incorporating rigid constraints between the car's sensors, pose convergence is significantly improved in terms of robustness. As the datasets used in this paper provide synchronized timestamps for the sensors, in contrast to the initial setup of MOISST, it is assumed here that there is no temporal shift between the sensors. Additionally, the vehicle trajectory is considered imperfect and is included in the optimized parameters along with the extrinsic calibration.
- SOAC [10]: When the initial error is too high, MOISST struggles to fuse the representations provided by the different sensors [10]. This could cause either duplication of structures or divergence in the calibration. To address these failure cases, SOAC assigns separate scene representations to each camera, ensuring data coherence within

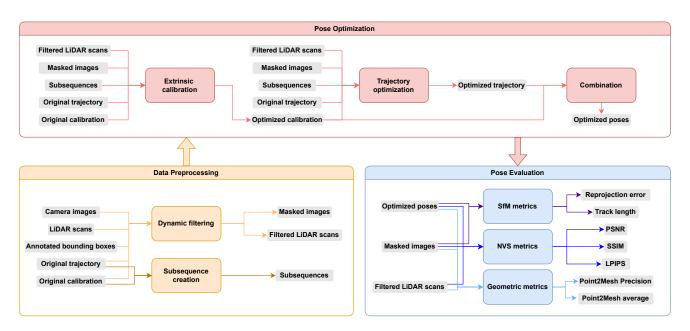


Fig. 2: **Pipeline:** First the data is preprocessed to remove dynamic elements, and create subsequences fitting our NeRF models. Then, the extrinsic parameters are optimized, followed by the trajectories. Finally, the new poses are evaluated.

each individual NeRF, while considering the overlap between sensors, which results in more reliable convergence to the correct calibration. Similarly to MOISST, we consider the system synchronized and add trajectory optimization.

- Nerfstudio [82]: We use the Nerfacto pose optimization method from Nerfstudio as a baseline for an independent pose optimization method that does not rely on rig calibration.
- 2) Notations: As the setup shares similarities with the ones from MOISST and SOAC, some of the notations are partially reused:
 - S: the set of sensors,
 - $_wT^i(t) \in \mathbf{R}^{4 \times 4}$: the pose of sensor $i \in S$ at time t in world coordinates,
 - $_{j}T^{i} \in \mathbf{R}^{4\times4}$: the transformation matrix from sensor i to sensor j.

The vehicle pose is associated with one sensor, designated as the reference sensor $r \in S$. A continuous trajectory of r, denoted \mathcal{T}_r , is constructed from the discrete poses of r using linear interpolation for the pose translation and spherical linear interpolation (SLERP [83]) for the rotation. This trajectory is expressed as a function of time, returning the pose of the reference sensor r for any given time t:

$$_{w}T^{r}(t) = \mathcal{T}_{r}(t) \tag{1}$$

From this, the pose of sensor i at time t can be obtained as:

$$_{w}T^{i}(t) = {}_{i}T^{r}\mathcal{T}_{r}(t). \tag{2}$$

Given the objective of optimizing both the extrinsic calibration and the reference trajectory, the function $E_{\rm cor}(i)$ is defined to provide the correction to the extrinsic calibration for sensor i, and $\mathcal{T}_{\rm cor}(t)$ is defined as the correction function

for the trajectory at time t. The optimized pose of sensor i at time t is then expressed as:

$$_{vv}T^{i}(t) = E_{cor}(i)_{i}T^{r}\mathcal{T}_{cor}(t)\mathcal{T}_{r}(t).$$
 (3)

For the extrinsic correction $E_{\rm cor}$, an embedding of size 6 is used to represent both the translation and rotation corrections in 3D space, with 3 dimensions dedicated to translation and 3 for rotation, using Rodrigues' rotation formula for the latter. By backpropagating through a shared calibration embedding, the multi-scene optimization process encourages convergence on a common optimal calibration across different scenes.

For trajectory correction \mathcal{T}_{cor} , superior performance was observed using the continuous representation proposed by Ma et al. [84], as opposed to embeddings. This method employs a multi-layer perceptron (MLP) to learn trajectory corrections based on input time. To prevent convergence to local minima, inspired by MOISST [9], we apply weight decay to the hash grids during the initial epochs to allow coarse-to-fine optimization.

In the extrinsic calibration optimization step, multiple instances of either MOISST or SOAC are employed, each assigned to a different subsequence, with an associated trajectory correction function \mathcal{T}_{cor} . The extrinsic calibration correction function E_{cor} is shared across all subsequences.

In the trajectory optimization step, the parameters of $E_{\rm cor}$ are held constant, and only the trajectory correction function $\mathcal{T}_{\rm cor}$ and the implicit scene representation are optimized.

C. Pose accuracy assessment

1) Triangulation metrics: We evaluate the improvement of our optimized poses against the original poses with keypoint triangulation using COLMAP [12]. Keypoint triangulation is a technique used in 3D reconstruction to estimate the 3D

coordinates of points in space based on their projections in multiple 2D images. First, distinct keypoints are extracted from the images, using SIFT features [13] in this case. Then these keypoints are matched across different views. Using these correspondences, COLMAP performs triangulation to compute the 3D positions of the keypoints. Unlike the usual COLMAP process, we do not refine the poses through bundle adjustment, as we want to evaluate the poses. We consider as a metric the average point reprojection error in pixels, which considers the distance between the reprojection of the 3D point in the image and the associated keypoint. We also consider the track length, which is the number of images in which a keypoint is tracked to a specific 3D point. While this evaluation focuses only on the camera poses and does not include LiDAR poses, it provides a highly reliable and precise measure of pose optimization. This is critical for ensuring the accuracy of the 3D reconstruction, even though the LiDAR data is not directly assessed in this step.

2) Novel View Synthesis: For the evaluation of novel view synthesis, we rely on multiple models: First, we use the NeRF model based on the model from MOISST with LiDAR supervision [9], that we call NeRF-LiDAR, but we omit the depth smoothness loss. Additionally, we use an appearance embedding inspired by NeRF-in-the-Wild [79] but instead of being image-specific, it is shared for all images from the same camera. Then, we also evaluate on the publicly available Nerfacto and Splatfacto models from Nerfstudio [82], with pose optimization deactivated. By doing so, we show that our results are not model specific, and provides improvements on publicly available models based on both NeRF [5] and 3D Gaussian Splatting [85]. As Nerfstudio pose optimization does not handle LiDAR scans, it is not evaluated on NeRF-LiDAR.

For the metrics, we evaluate the PSNR, SSIM and LPIPS metrics after training the models with the original and optimized poses. As we optimize our poses through NeRF training, it appears natural that the NVS task should provide the most constant improvement in the metrics.

3) Geometric consistency: For geometric consistency, we used the Delauney mesher in COLMAP to create a 3D mesh that we compare to the accumulated LiDAR pointcloud. To evaluate the geometry, we rely on two metrics from [74]: We compare the mean distance from the accumulated LiDAR pointcloud to the mesh (noted P→M for point-to-mesh) and the percentage of points with distance under 15 cm (noted Prec. for precision) as an evaluation of the consistency of our calibration and trajectory optimization, as we assume that a better alignment between the LiDAR and the cameras should also provide a better alignment between the LiDAR scans and the surface built from the images. As mentioned previously, Nerfstudio pose optimization not handling LiDAR scans means that it is not evaluated on these metrics.

IV. EXPERIMENTAL SETUP

A. Datasets

In this paper, we evaluate the optimized poses with our pipeline compared to the original poses on 4 widely used publicly available autonomous driving datasets:

- 1) KITTI-360 Dataset [2]: The KITTI-360 dataset was captured in and around the city of Karlsruhe, Germany, covering both urban and suburban areas. It extends the original KITTI dataset [86] with 360° panoramic imagery and offers high-resolution data from 4 cameras, a 32-beam LiDAR, and GPS/IMU sensors. The diverse range of driving environments, from city streets to rural roads, allows researchers to address tasks such as 3D object detection, semantic segmentation, and scene flow estimation with a focus on real-world driving conditions. The provided 6-DoF poses are derived using a combination of LiDAR-based SLAM and SfM techniques, refined via global optimization and loop closures to ensure consistent, accurate localization.
- 2) NuScenes Dataset [4]: The NuScenes dataset was collected across the urban streets of Boston and Singapore, ensuring a wide variety of driving conditions and environments. With 6 cameras, a 32-beam LiDAR, radar sensors, and GPS/IMU data, the dataset captures complex scenes that include both dense urban areas and more sparse suburban roads. The 1,000 driving scenes, each 20 seconds long, cover day and night conditions, providing valuable data for 3D object detection, tracking, and sensor fusion research. The dataset supplies global vehicle poses computed by fusing high-precision GPS/IMU data an HD map created using the LiDAR scans, which is why the poses are defined in SE2.
- 3) PandaSet [3]: Captured primarily in urban environments across several cities in China, the PandaSet dataset is part of Baidu's Apollo project and includes data from high-definition sensors such as 5 cameras, a 64-beam LiDAR, and radar. The dataset's rich urban and suburban setting provides data for tasks like 3D object detection and sensor fusion. The real-world driving scenarios include busy city intersections, highways, and residential streets, offering diverse challenges for autonomous driving models. PandaSet obtains poses through robust localization pipelines that integrate information from LiDAR, cameras, inertial sensors and GNSS, using LiDAR SLAM methods followed by post-processing for enhanced consistency.
- 4) Waymo Open Dataset [1]: The Waymo Open Dataset was gathered from the streets of Phoenix, Arizona, where Waymo's fleet of self-driving vehicles operates in various urban and suburban environments. The dataset contains over 1000 hours of data, recorded using 5 LiDAR sensors, 5 cameras, and additional sensors. This diverse data, covering both residential neighborhoods and busy city streets, provides ground truth for tasks such as 3D object detection, tracking, and prediction, while also accounting for various lighting and weather conditions. Waymo leverages its advanced, in-house localization system, fusing data from high-resolution LiDAR, IMU, and additional sensors to deliver extremely accurate 6-DoF poses in a global reference frame.

B. Subsequence Creation

Given the large size of the datasets and the computational demands of training NeRF models, we report the results from subsets of each dataset to ensure efficient processing. The selection process was designed to be systematic, avoiding any bias from hand-picked sequences. The subsequences were created as follows:

- **KITTI-360**: Subsequencies of 50 meters are constructed starting from frame 500 of sequences **0005**, **0006**, **0007**, **0009**, **0010**. This results in 50 subsequences, each covering 50 meters, for a total of 2.5 kilometers.
- NuScenes: The first 30 meters of the first 10 sequences are used.
- PandaSet: We select the first 10 sequences with available semantic labels (sequences 001, 002, 003, 005, 011, 013, 015, 016, 017, 019).
- Waymo Open Dataset: The first 50 meters from 10 entirely static sequences are extracted, identified through annotated bounding boxes (sequences segment-10061, segment-10676, segment-11379, segment-11724, segment-12879, segment-13085, segment-13142, segment-13196, segment-14004, segment-14869).

For each dataset, we optimize the poses of the cameras and the 360° LiDAR. Dynamic masks are generated for KITTI-360, NuScenes, and PandaSet using the provided annotations. As stated in Waymo's paper, the fleet of vehicles used results in changing cars for capture between sequences, which also leads to differences in extrinsic calibration. Therefore, in this case, we optimize the calibration and trajectory for each subsequence individually, rather than applying a multiscene calibration approach (Cf. III-A).

C. Optimization hyperparameters

The image downscale factors and number of epochs or steps for each process of the pipeline is detailed in Table I.

Parameter	Dataset	MOISST	SOAC			
Optimization	KITTI-360	2	4			
downscale	NuScenes	4	6			
factor	PandaSet	4	6			
	Waymo	4	6			
Optimization iterations	All	15 epo	ochs			
NeRF-LiDAR	KITTI-360	1				
NVS downscale	NuScenes	2				
factor	PandaSet	2				
	Waymo	2				
NeRF-LiDAR NVS iterations	All	10 epochs				
Nerfstudio	All	1				
downscale factor	7 111	1				
Nerfstudio iterations	All	30k st	eps			

TABLE I: **Hyperparameters:** the images are downscaled for MOISST and SOAC during optimization to reduce training time and memory usage.

V. EXPERIMENTAL RESULTS

The poses obtained through the pipeline by using either MOISST and SOAC are evaluated with the metrics mentioned in III-C. For NuScenes, the provided poses do not have any information on the Z-axis. In order to retrieve an approximate value on the Z-axis before optimizing, KISS-ICP [19] is used before running MOISST and SOAC. The results using KISS-ICP are shown in Table III for fairness to prove that the

improvement mainly comes from MOISST and SOAC, and not because we preprocess with KISS-ICP.

A. Triangulation metrics

In Table IIa are reported the quantitative results of the COLMAP metrics (reprojection error and track length) between the original poses, and poses optimized with MOISST or SOAC. An overall improvement can be observed with MOISST over the original poses, although the improvement for KITTI-360 is minimal in absolute terms (1.5% for reprojection error and 2.3% for track length for KITTI-360 vs $10\% \sim 36\%$ and $6.6\% \sim 33\%$ for the 3 other datasets). For SOAC, we see a regression on KITTI-360 and Waymo, while progress is still noticeable on NuScenes and PandaSet, though less pronounced than for MOISST.

Per sequence difference with the original poses for different metrics for MOISST and SOAC are provided for each dataset in Fig. 9, Fig. 10, Fig. 11 and Fig. 12. A closer inspection reveals that for KITTI-360 (Fig. 9), the improvement in the reprojection metric for MOISST is not consistent across all sequences (improvement in 24/50 subsequences). While an increase in track length is observable overall (improvement in 41/50 subsequences), the absolute values remain small, which aligns with the values from Table II. Both MOISST and SOAC show consistent improvements on NuScenes and PandaSet (Cf. Fig. 10 and Fig. 11). However, SOAC results are worse on KITTI-360 (improvement in 0/50 and 6/50 subsequences) and Waymo (improvement in 0/10 and 2/10 subsequences) (Cf. Fig 9 and Fig.12).

B. Novel View Synthesis

For NVS evaluation, we train the NeRF-LiDAR model with 1 out of 2 frames, and evaluate on the other. For Nerfstudio models, the default interval mode is used to split the training and evaluation sets, with 1 out of 8 frames for evaluation. The novel view synthesis metrics (PSNR, SSIM, LPIPS) are reported in Table IIb, Table IIc and Table IId. MOISST provides the best results across all metrics (an improvement of $0.6\% \sim 15\%$ on PSNR, $0.6\% \sim 12\%$ on SSIM and $2.4\% \sim 33\%$ on LPIPS) on all four datasets. The second best depends on the dataset. For KITTI-360, SOAC actually performs worse than the original poses. As for NuScenes, PandaSet and Waymo, the second best is either SOAC or Nerfstudio, showing that different optimization methods are able to improve the original poses on these metrics. Per sequence difference with the original poses for different metrics for MOISST and SOAC are provided for each dataset in Fig. 17, Fig. 18, Fig. 19 and Fig. 20. Qualitative results with rendering images from different methods are provided in Fig. 3 and Fig. 5. We observe that MOISST provides the best quality in terms of details and fine structures. The improvement of the geometry can be seen in Fig. 4, the road is flatter, and the fine structures are better reconstructed.

C. Geometric consistency

In Table IIe are reported the surface metrics computed by calculating the distance between the Delauney mesh and the

		Reproject	ion error↓		Track length↑				
	Original	MOISST	SOAC	Nerfstudio	Original	MOISST	SOAC	Nerfstudio	
KITTI-360	0.586	0.577	0.735	0.691	6.53	6.68	6.48	6.55	
NuScenes	1.339	0.852	1.016	1.166	5.40	7.20	6.60	6.59	
PandaSet	1.187	0.981	1.020	1.284	6.32	6.86	6.75	6.44	
Waymo	1.137	1.015	1.344	1.466	5.73	6.11	5.19	5.51	

(a) Colmap metrics

	PSNR↑				SSIM↑		LPIPS↓			
	Original	MOISST	SOAC	Original	MOISST	SOAC	Original	MOISST	SOAC	
KITTI-360	22.42	22.61	22.28	0.829	0.834	0.824	0.283	0.272	0.295	
NuScenes	22.34	23.46	23.12	0.810	0.851	0.843	0.465	0.339	0.370	
PandaSet	22.08	22.36	22.32	0.788	0.803	0.800	0.482	0.433	0.441	
Waymo	24.56	25.03	24.63	0.848	0.857	0.849	0.468	0.420	0.466	

(b) NVS NeRF-LiDAR

	PSNR↑			SSIM↑				LPIPS↓				
	Original	MOISST	SOAC	Nerfstudio	Original	MOISST	SOAC	Nerfstudio	Original	MOISST	SOAC	Nerfstudio
KITTI-360	21.24	21.37	21.05	21.24	0.713	0.720	0.700	0.710	0.281	0.274	0.294	0.284
NuScenes	20.41	21.68	21.41	21.61	0.696	0.778	0.756	0.765	0.545	0.400	0.436	0.422
PandaSet	21.60	22.40	22.34	22.14	0.686	0.723	0.718	0.710	0.517	0.461	0.472	0.484
Waymo	23.54	24.54	23.95	24.40	0.750	0.772	0.755	0.767	0.493	0.450	0.489	0.465

(c) NVS Nerfacto

	PSNR↑			SSIM↑				LPIPS↓				
	Original	MOISST	SOAC	Nerfstudio	Original	MOISST	SOAC	Nerfstudio	Original	MOISST	SOAC	Nerfstudio
KITTI-360	23.40	23.63	22.99	23.13	0.757	0.764	0.743	0.747	0.223	0.216	0.235	0.228
NuScenes	22.29	25.66	24.77	24.65	0.762	0.852	0.825	0.819	0.397	0.264	0.297	0.302
PandaSet	23.22	24.31	24.11	23.38	0.770	0.811	0.802	0.767	0.323	0.286	0.294	0.325
Waymo	24.06	25.85	23.69	24.66	0.788	0.819	0.777	0.785	0.407	0.346	0.424	0.393

(d) NVS Splatfacto

	ĺ	Prec. ↑		1	$P \rightarrow M (m) \downarrow$	
	Original	MOISST	SOAC	Original	MOISST	SOAC
KITTI-360	0.589	0.600	0.582	0.254	0.228	0.261
NuScenes	0.422	0.673	0.632	0.296	0.129	0.136
PandaSet	0.385	0.400	0.393	0.378	0.355	0.357
Waymo	0.441	0.626	0.417	0.408	0.340	0.386

(e) Delauney mesh metrics

TABLE II: Quantitative results: The best result in **bold**, the second best <u>underlined</u>.

Met	ric	Original	ICP	MOISST	SOAC
Colmap	Reproj error	1.339	1.306	0.852	1.016
Comap	Track length	5.40	5.41	7.20	6.60
	PSNR	22.34	22.76	23.46	23.12
NeRF-LiDAR	SSIM	0.810	0.823	0.851	0.843
	LPIPS	0.465	0.418	0.339	0.370
	PSNR	20.41	20.54	21.68	21.41
Nerfacto	SSIM	0.696	0.701	0.778	0.756
	LPIPS	0.545	0.531	0.400	0.436
	PSNR	22.29	23.05	25.66	24.77
Splatfacto	SSIM	0.762	0.774	0.852	0.825
	LPIPS	0.397	0.365	0.264	0.297
Delauney	Prec.	0.422	0.508	0.673	0.632
Detautiey	$P \rightarrow M$	0.296	0.171	0.129	0.136

TABLE III: **NuScenes metrics:** KISS-ICP [19] (ICP) improves compared to Original, while still providing inferior metrics to MOISST or SOAC. The best result in **bold**, the second best underlined.

accumulated LiDAR point cloud. MOISST performs better in all datasets. When we analyze the per sequence changes in

Fig. 13, Fig. 14, Fig. 15 and Fig. 16 we can see an overall improvement on all the datasets with MOISST, while SOAC is worse on KITTI-360 and have a less consistent improvement on Waymo (improvement in 6/10 subsequences). Fig. 6 shows the Delauney mesh from the original and optimized poses in a NuScenes sequence. The surface of the road, as well as the structures (trees, poles) are much better defined. It illustrates how inaccurate the original poses are and the substantial improvement brought by our method.

D. Discussion

Overall, MOISST outperforms SOAC in most scenarios. SOAC was originally designed to enhance robustness when sensor fusion struggles due to high initial noise [10], but in our case, we start from the provided calibration parameters, which are supposedly significantly more accurate than the noise levels assumed in the original SOAC paper (50cm translation error and 5° rotation error on all axis). Thus, the fusion of information from all the sensors in a NeRF is

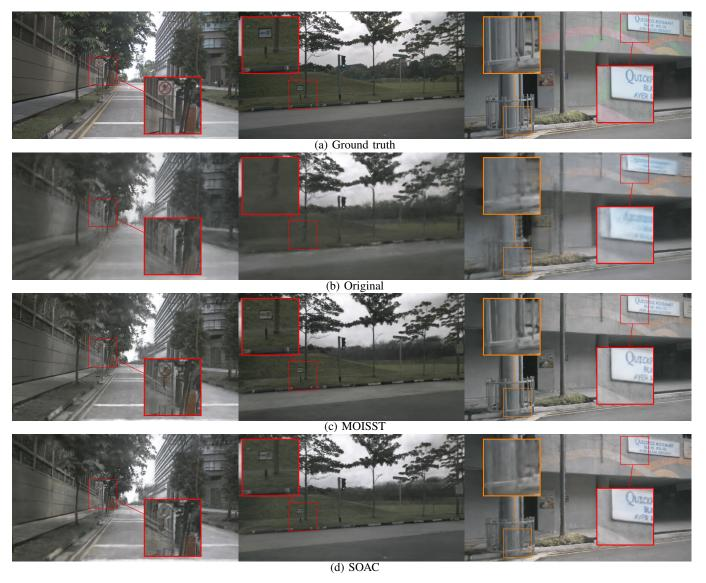


Fig. 3: NuScenes NeRF-LiDAR Novel View Synthesis

much easier, largely reducing the usefulness of using SOAC instead of MOISST. Additionally, SOAC relies on higher image downscale factors to manage the exponential training time required for multiple NeRF models, each trained on a single camera's observation, which can adversely affect the quality of the reconstructed scene. The performance of the Nerfstudio pose optimization varies depending on the dataset, while always being below MOISST. Adding to the fact that it cannot handle LiDAR data, this proves the advantages of using MOISST in this setup, being more performant and versatile.

Analyzing the improvements provided by MOISST relative to the original dataset poses, we observe that KITTI-360 shows the smallest absolute change, which underscores the high precision of its original poses. In contrast, NuScenes, which lacks Z-axis information, benefits the most from the optimization, yielding significant quantitative and qualitative enhancements (Cf. Table II, Fig. 3 and Fig. 6).

E. Optimal pose selection

Based on the evaluation metrics previously introduced, a sign agreement matrix can be constructed for each dataset (Cf. Fig. 8). The agreement score, ranging from 0 to 1, indicates the proportion of instances where a pair of metrics agree on whether there is an improvement or regression compared to the original poses, calculated on the cumulated results of MOISST and SOAC poses.

Upon examining these matrices, there is an overall agreement that is over 0.5, showing that improving a metric correlates with the improvement of the other metrics and viceversa. The lowest overall agreement being for KITTI-360 is reasonable, as the absolute improvement is the lowest, making the refinement less obvious across the metrics.

In practical cases, the user can select the optimal poses between the original and the optimized ones with a simple majority vote, or ponder the metrics depending on the needs.

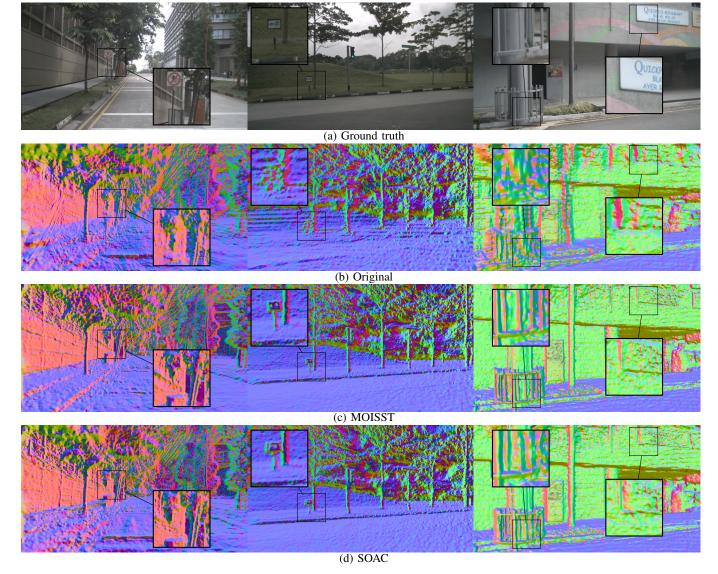


Fig. 4: NuScenes NeRF-LiDAR Novel View Synthesis normal maps

F. Limitations

Since our pose optimization method depends on 3D reconstruction using a NeRF model, it inherits the same limitations. Specifically, the NeRF model may struggle to produce high-quality geometry in certain scenarios. Common challenges include night scenes, where most features are too dim to be detected, as well as environments with repetitive or absent features, such as continuous walls or tunnels (Cf. Fig.7a). In these cases, the model is still able to rely on the LiDAR scans for geometry on covered parts, which helps to mitigate complete divergence. Additionally, structures located far beyond the bounds of the NeRF scene cannot be reconstructed, making them unreliable for pose optimization (Cf. Fig.7b).

VI. CONCLUSION

This work introduces a method for optimizing sensor poses and calibration parameters, placing a strong emphasis on rigorous evaluation using a variety of metrics. Our comprehensive evaluation demonstrates significant improvements in the optimized outputs when using the MOISST model, which in turn should enhance the accuracy of downstream tasks such as sensor fusion, 3D reconstruction, and localization, ultimately benefiting the broader research community.

Furthermore, it shows the necessity of acknowledging that the evaluation data itself may sometimes contain inherent inaccuracies. Therefore, when observed variations in performance metrics are minimal, it may indicate that the limitations stem from the precision of the underlying dataset rather than a lack of significant improvement. This insight underscores the importance of refining not only the models and methods but also the evaluation standards and dataset quality to ensure truly reliable comparisons.

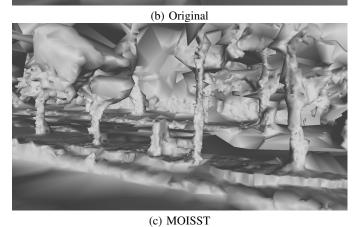
By making these optimized poses and calibration parameters publicly available, we aim to support future research, fostering the development of more robust models and enhancing the overall reliability of results across the field.



Fig. 5: PandaSet Nerfstudio Novel View Synthesis



(a) Ground truth



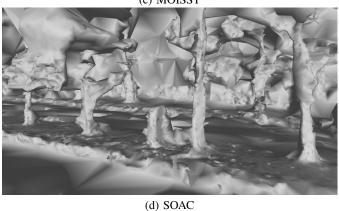


Fig. 6: Delauney mesh on NuScenes sequence.



(a) It is very dark inside the tunnel, with a bright light at the end. The model is unable to find distinctive features.



(b) The scene exhibits highly repetitive elements, such as the green grass, and includes distant structures beyond the bounds of the NeRF model. Additionally, the sun flare introduces further complications.

Fig. 7: Examples of challenging cases.

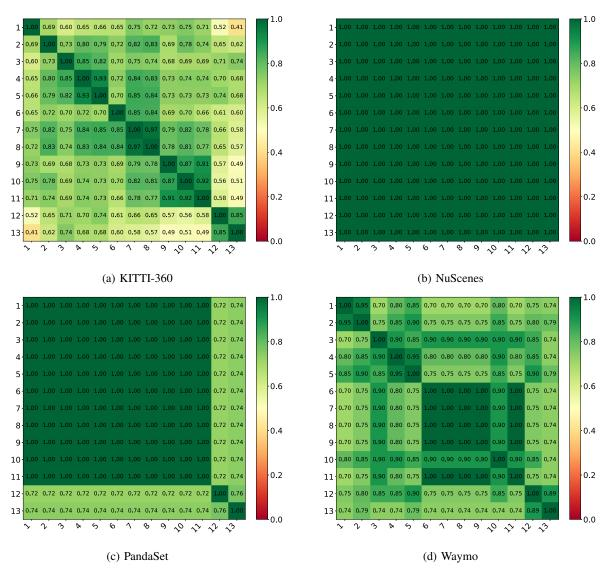


Fig. 8: **Sign agreement matrices:** on all the metrics for each dataset. (1) Colmap reprojection, (2) Colmap track length (3) MOISST* PSNR (4) MOISST* SSIM (5) MOISST* LPIPS (6) Nerfacto PSNR (7) Nerfacto SSIM (8) Nerfacto LPIPS (9) Splatfacto PSNR (10) Splatfacto SSIM (11) Splatfacto LPIPS (12) Delauney Prec. (13) Delauney P→M.

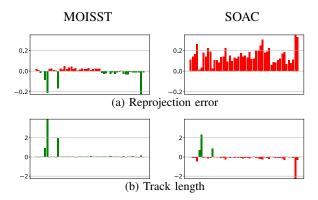


Fig. 9: KITTI-360 Colmap metrics vs original poses (improvement in green, regression in red).

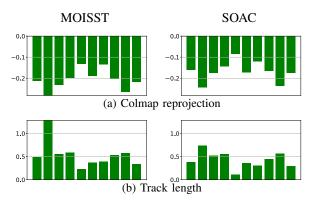


Fig. 11: Pandaset Colmap metrics vs original poses (improvement in green, regression in red).

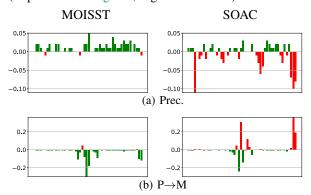


Fig. 13: KITTI-360 Delauney metrics vs original poses (improvement in green, regression in red).

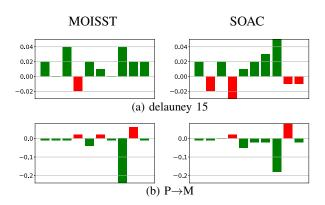


Fig. 15: Pandaset Delauney metrics vs original poses (improvement in green, regression in red).

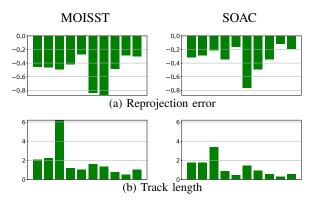


Fig. 10: NuScenes Colmap metrics vs original poses (improvement in green, regression in red).

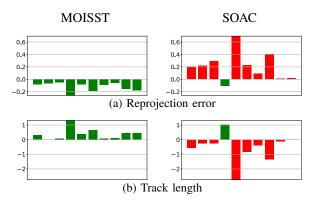


Fig. 12: Waymo Colmap metrics vs original poses (improvement in green, regression in red).

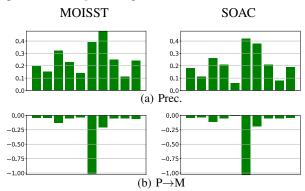


Fig. 14: NuScenes Delauney metrics vs original poses (improvement in green, regression in red).

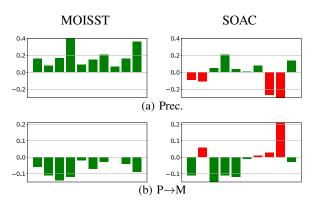


Fig. 16: Waymo Delauney metrics vs original poses (improvement in green, regression in red).

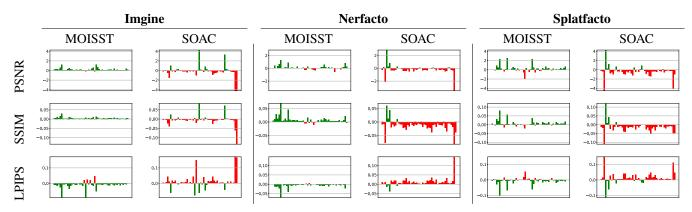


Fig. 17: KITTI-360 NVS metrics vs original poses (improvement in green, regression in red).

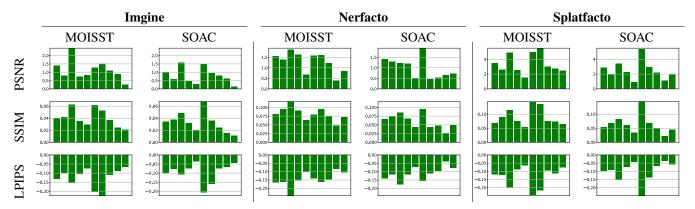


Fig. 18: NuScenes NVS metrics vs original poses (improvement in green, regression in red).

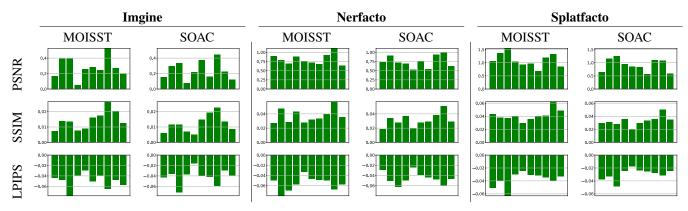


Fig. 19: Pandaset NVS metrics vs original poses (improvement in green, regression in red).

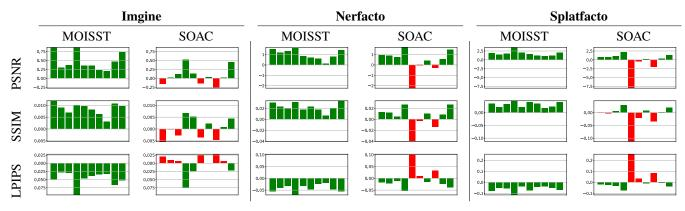


Fig. 20: Waymo NVS metrics vs original poses (improvement in green, regression in red).

REFERENCES

- P. Sun, H. Kretzschmar, X. Dotiwalla, A. Chouard, V. Patnaik, P. Tsui, J. Guo, Y. Zhou, Y. Chai, B. Caine et al., "Scalability in perception for autonomous driving: Waymo open dataset," in *IEEE/CVF Conference* on Computer Vision and Pattern Recognition (CVPR), 2020, pp. 2446– 2454
- [2] Y. Liao, J. Xie, and A. Geiger, "KITTI-360: A novel dataset and benchmarks for urban scene understanding in 2d and 3d," *IEEE Transactions on Pattern Analysis and Machine Intelligence (TPAMI)*, vol. 45, no. 3, pp. 3292–3310, 2022.
- [3] P. Xiao, Z. Shao, S. Hao, Z. Zhang, X. Chai, J. Jiao, Z. Li, J. Wu, K. Sun, K. Jiang et al., "Pandaset: Advanced sensor suite dataset for autonomous driving," in *IEEE International Intelligent Transportation Systems Conference (ITSC)*, 2021, pp. 3095–3101.
- [4] H. Caesar, V. Bankiti, A. H. Lang, S. Vora, V. E. Liong, Q. Xu, A. Krishnan, Y. Pan, G. Baldan, and O. Beijbom, "nuscenes: A multimodal dataset for autonomous driving," in *IEEE/CVF Conference on Computer Vision and Pattern Recognition (CVPR)*, 2020, pp. 11621–11631.
- [5] B. Mildenhall, P. P. Srinivasan, M. Tancik, J. T. Barron, R. Ramamoorthi, and R. Ng, "NeRF: Representing scenes as neural radiance fields for view synthesis," *Communications of the ACM*, vol. 65, no. 1, pp. 99– 106, 2021.
- [6] Z. Wang, S. Wu, W. Xie, M. Chen, and V. A. Prisacariu, "Nerf-: Neural radiance fields without known camera parameters," arXiv preprint arXiv:2102.07064, 2021.
- [7] C.-H. Lin, W.-C. Ma, A. Torralba, and S. Lucey, "Barf: Bundle-adjusting neural radiance fields," in *IEEE/CVF international conference on computer vision (ICCV)*, 2021.
- [8] S. Zhou, S. Xie, R. Ishikawa, K. Sakurada, M. Onishi, and T. Oishi, "INF: Implicit Neural Fusion for LiDAR and Camera," in *IEEE/RSJ International Conference on Intelligent Robots and Systems (IROS)*, 2023, pp. 10918–10925.
- [9] Q. Herau, N. Piasco, M. Bennehar, L. Roldão, D. Tsishkou, C. Migniot, P. Vasseur, and C. Demonceaux, "MOISST: Multimodal Optimization of Implicit Scene for SpatioTemporal calibration," in *IEEE/RSJ Interna*tional Conference on Intelligent Robots and Systems (IROS), 2023, pp. 1810–1817.
- [10] Q. Herau, N. Piasco, M. Bennehar, L. Roldao, D. Tsishkou, C. Migniot, P. Vasseur, and C. Demonceaux, "Soac: Spatio-temporal overlap-aware multi-sensor calibration using neural radiance fields," in *IEEE/CVF* Conference on Computer Vision and Pattern Recognition (CVPR), 2024, pp. 15131–15140.
- [11] Z. Yang, G. Chen, H. Zhang, K. Ta, I. A. Bârsan, D. Murphy, S. Mani-vasagam, and R. Urtasun, "Unical: Unified neural sensor calibration," in European conference on computer vision (ECCV), 2025, pp. 327–345.
- [12] J. L. Schönberger and J.-M. Frahm, "Structure-from-Motion Revisited," in *IEEE/CVF Conference on Computer Vision and Pattern Recognition* (CVPR), 2016, pp. 4104–4113.
- [13] D. G. Lowe, "Distinctive image features from scale-invariant keypoints," International journal of computer vision (IJCV), vol. 60, pp. 91–110, 2004.
- [14] D. Nistér, O. Naroditsky, and J. Bergen, "Visual odometry," in IEEE/CVF Conference on Computer Vision and Pattern Recognition (CVPR), vol. 1, 2004, pp. I–I.
- [15] H.-J. Chien, C.-C. Chuang, C.-Y. Chen, and R. Klette, "When to use what feature? sift, surf, orb, or a-kaze features for monocular visual odometry," in *IEEE International Conference on Image and Vision Computing New Zealand (IVCNZ)*, 2016, pp. 1–6.
- [16] H. Durrant-Whyte and T. Bailey, "Simultaneous localization and mapping: part i," *IEEE robotics & automation magazine*, vol. 13, no. 2, pp. 99–110, 2006.
- [17] R. Mur-Artal, J. M. M. Montiel, and J. D. Tardos, "Orb-slam: a versatile and accurate monocular slam system," *IEEE transactions on robotics (T-RO)*, vol. 31, no. 5, pp. 1147–1163, 2015.
- [18] K. S. Arun, T. S. Huang, and S. D. Blostein, "Least-squares fitting of two 3-d point sets," *IEEE Transactions on Pattern Analysis and Machine Intelligence (TPAMI)*, no. 5, pp. 698–700, 1987.
- [19] I. Vizzo, T. Guadagnino, B. Mersch, L. Wiesmann, J. Behley, and C. Stachniss, "Kiss-icp: In defense of point-to-point icp-simple, accurate, and robust registration if done the right way," *IEEE Robotics and Automation Letters (RA-L)*, vol. 8, no. 2, pp. 1029–1036, 2023.
- [20] Z. Zhang and S. Singh, "Loam: Lidar odometry and mapping in realtime," in *IEEE/RSJ International Conference on Intelligent Robots and Systems (IROS)*, 2014, pp. 2171–2176.

- [21] T. Shan and B. Englot, "Lego-loam: Lightweight and ground-optimized lidar odometry and mapping on variable terrain," in *IEEE/RSJ Interna*tional Conference on Intelligent Robots and Systems (IROS), 2018, pp. 4758–4765.
- [22] H. Wang, C. Wang, C.-L. Chen, and L. Xie, "F-loam: Fast lidar odometry and mapping," in *IEEE/RSJ International Conference on Intelligent Robots and Systems (IROS)*, 2021, pp. 4390–4396.
- [23] J. Zhang and S. Singh, "Visual-lidar odometry and mapping: Low-drift, robust, and fast," in *IEEE international conference on robotics and automation (ICRA)*, 2015, pp. 2174–2181.
- [24] J. Graeter, A. Wilczynski, and M. Lauer, "Limo: Lidar-monocular visual odometry," in *IEEE/RSJ international conference on intelligent robots* and systems (IROS), 2018, pp. 7872–7879.
- [25] Y. Zhu, C. Zheng, C. Yuan, X. Huang, and X. Hong, "Camvox: A low-cost and accurate lidar-assisted visual slam system," in *IEEE International Conference on Robotics and Automation (ICRA)*, 2021, pp. 5049–5055.
- [26] C.-C. Chou and C.-F. Chou, "Efficient and accurate tightly-coupled visual-lidar slam," *IEEE Transactions on Intelligent Transportation* Systems (ITSC), vol. 23, no. 9, pp. 14509–14523, 2021.
- [27] S.-S. Huang, Z.-Y. Ma, T.-J. Mu, H. Fu, and S.-M. Hu, "Lidar-monocular visual odometry using point and line features," in *IEEE international* conference on robotics and automation (ICRA), 2020, pp. 1091–1097.
- [28] Y.-S. Shin, Y. S. Park, and A. Kim, "Dvl-slam: Sparse depth enhanced direct visual-lidar slam," *Autonomous Robots*, vol. 44, no. 2, pp. 115– 130, 2020.
- [29] Z. Yuan, Q. Wang, K. Cheng, T. Hao, and X. Yang, "Sdv-loam: semi-direct visual-lidar odometry and mapping," *IEEE Transactions on Pattern Analysis and Machine Intelligence (TPAMI)*, vol. 45, no. 9, pp. 11203–11220, 2023.
- [30] S. Wang, R. Clark, H. Wen, and N. Trigoni, "Deepvo: Towards end-to-end visual odometry with deep recurrent convolutional neural networks," in *IEEE international conference on robotics and automation (ICRA)*, 2017, pp. 2043–2050.
- [31] D. DeTone, T. Malisiewicz, and A. Rabinovich, "Superpoint: Self-supervised interest point detection and description," in *IEEE/CVF Conference on Computer Vision and Pattern Recognition Workshops* (CVPRW), 2018, pp. 224–236.
- [32] P.-E. Sarlin, D. DeTone, T. Malisiewicz, and A. Rabinovich, "Superglue: Learning feature matching with graph neural networks," in *IEEE/CVF Conference on Computer Vision and Pattern Recognition (CVPR)*, 2020, pp. 4938–4947.
- [33] J. Wang, N. Karaev, C. Rupprecht, and D. Novotny, "Vggsfm: Visual geometry grounded deep structure from motion," in *IEEE/CVF Confer*ence on Computer Vision and Pattern Recognition (CVPR), 2024, pp. 21 686–21 697.
- [34] S. Wang, V. Leroy, Y. Cabon, B. Chidlovskii, and J. Revaud, "Dust3r: Geometric 3d vision made easy," in *IEEE/CVF Conference on Computer Vision and Pattern Recognition (CVPR)*, 2024, pp. 20697–20709.
- [35] V. Leroy, Y. Cabon, and J. Revaud, "Grounding image matching in 3d with mast3r," in *European conference on computer vision (ECCV)*, 2024, pp. 71–91.
- [36] G. Wang, X. Wu, S. Jiang, Z. Liu, and H. Wang, "Efficient 3d deep lidar odometry," *IEEE Transactions on Pattern Analysis and Machine Intelligence (TPAMI)*, vol. 45, no. 5, pp. 5749–5765, 2022.
- [37] W. Lu, G. Wan, Y. Zhou, X. Fu, P. Yuan, and S. Song, "Deepvcp: An end-to-end deep neural network for point cloud registration," in IEEE/CVF international conference on computer vision (ICCV), October 2019.
- [38] Y. Jia, H. Luo, F. Zhao, G. Jiang, Y. Li, J. Yan, Z. Jiang, and Z. Wang, "Lvio-fusion: A self-adaptive multi-sensor fusion slam framework using actor-critic method," in *IEEE/RSJ international conference on intelligent* robots and systems (IROS), 2021, pp. 286–293.
- [39] B. Li, M. Hu, S. Wang, L. Wang, and X. Gong, "Self-supervised visuallidar odometry with flip consistency," in *IEEE/CVF Winter Conference* on Applications of Computer Vision (WACV), 2021, pp. 3844–3852.
- [40] Y. Jeong, S. Ahn, C. Choy, A. Anandkumar, M. Cho, and J. Park, "Self-calibrating neural radiance fields," in *IEEE/CVF international conference on computer vision (ICCV)*, 2021, pp. 5741–5751.
- [41] W. Bian, Z. Wang, K. Li, J.-W. Bian, and V. A. Prisacariu, "Nopenerf: Optimising neural radiance field with no pose prior," in *IEEE/CVF Conference on Computer Vision and Pattern Recognition (CVPR)*, 2023, pp. 4160–4169.
- [42] I. Kim, M. Choi, and H. J. Kim, "Up-nerf: Unconstrained pose prior-free neural radiance field," Advances in neural information processing systems (NeurIPS), vol. 36, 2024.

- [43] M. Caron, H. Touvron, I. Misra, H. Jégou, J. Mairal, P. Bojanowski, and A. Joulin, "Emerging properties in self-supervised vision transformers," in *IEEE/CVF international conference on computer vision (ICCV)*, 2021, pp. 9650–9660.
- [44] E. Sucar, S. Liu, J. Ortiz, and A. Davison, "iMAP: Implicit Mapping and Positioning in Real-Time," in *IEEE/CVF international conference* on computer vision (ICCV), 2021, pp. 6229–6238.
- [45] Z. Zhu, S. Peng, V. Larsson, W. Xu, H. Bao, Z. Cui, M. R. Oswald, and M. Pollefeys, "Nice-slam: Neural implicit scalable encoding for slam," in *IEEE/CVF Conference on Computer Vision and Pattern Recognition* (CVPR), 2022, pp. 12786–12796.
- [46] C.-M. Chung, Y.-C. Tseng, Y.-C. Hsu, X.-Q. Shi, Y.-H. Hua, J.-F. Yeh, W.-C. Chen, Y.-T. Chen, and W. H. Hsu, "Orbeez-slam: A real-time monocular visual slam with orb features and nerf-realized mapping," in *IEEE International Conference on Robotics and Automation (ICRA)*, 2023, pp. 9400–9406.
- [47] R. Mur-Artal and J. D. Tardós, "Orb-slam2: An open-source slam system for monocular, stereo, and rgb-d cameras," *IEEE transactions on robotics* (*T-RO*), vol. 33, no. 5, pp. 1255–1262, 2017.
- [48] A. Rosinol, J. J. Leonard, and L. Carlone, "Nerf-slam: Real-time dense monocular slam with neural radiance fields," in *IEEE/RSJ International Conference on Intelligent Robots and Systems (IROS)*, 2023, pp. 3437–3444.
- [49] T. Deng, G. Shen, T. Qin, J. Wang, W. Zhao, J. Wang, D. Wang, and W. Chen, "Plgslam: Progressive neural scene representation with local to global bundle adjustment," in *IEEE/CVF Conference on Computer Vision and Pattern Recognition (CVPR)*, 2024, pp. 19657–19666.
- [50] X. Zhong, Y. Pan, J. Behley, and C. Stachniss, "Shine-mapping: Large-scale 3d mapping using sparse hierarchical implicit neural representations," in *IEEE International Conference on Robotics and Automation (ICRA)*, 2023, pp. 8371–8377.
- [51] J. Deng, Q. Wu, X. Chen, S. Xia, Z. Sun, G. Liu, W. Yu, and L. Pei, "Nerf-loam: Neural implicit representation for large-scale incremental lidar odometry and mapping," in *IEEE/CVF international conference* on computer vision (ICCV), 2023, pp. 8218–8227.
- [52] S. Isaacson, P.-C. Kung, M. Ramanagopal, R. Vasudevan, and K. A. Skinner, "Loner: Lidar only neural representations for real-time slam," *IEEE Robotics and Automation Letters (RA-L)*, 2023.
- [53] Y. Pan, X. Zhong, L. Wiesmann, T. Posewsky, J. Behley, and C. Stachniss, "Pin-slam: Lidar slam using a point-based implicit neural representation for achieving global map consistency," *IEEE Transactions on Robotics (T-RO)*, vol. 40, pp. 4045–4064, 2024.
- [54] X. Liu, Y. Li, Y. Teng, H. Bao, G. Zhang, Y. Zhang, and Z. Cui, "Multi-modal neural radiance field for monocular dense slam with a light-weight tof sensor," in *IEEE/CVF international conference on computer vision (ICCV)*, 2023, pp. 1–11.
- [55] H. Zhang, Y. Zou, Z. Yan, and H. Cheng, "Rapid-mapping: Lidar-visual implicit neural representations for real-time dense mapping," IEEE Robotics and Automation Letters (RA-L), 2024.
- [56] Z. Zhang, "A flexible new technique for camera calibration," *IEEE Transactions on Pattern Analysis and Machine Intelligence (TPAMI)*, vol. 22, no. 11, pp. 1330–1334, 2000.
- [57] Q. Zhang and R. Pless, "Extrinsic calibration of a camera and laser range finder (improves camera calibration)," in *IEEE/RSJ International Conference on Intelligent Robots and Systems (IROS)*, vol. 3, 2004, pp. 2301–2306.
- [58] A. Geiger, F. Moosmann, Ö. Car, and B. Schuster, "Automatic camera and range sensor calibration using a single shot," in *IEEE international* conference on robotics and automation (RA-L), 2012, pp. 3936–3943.
- [59] C. Guindel, J. Beltrán, D. Martín, and F. García, "Automatic extrinsic calibration for lidar-stereo vehicle sensor setups," in *IEEE international* conference on intelligent transportation systems (ITSC), 2017, pp. 1–6.
- [60] Z. Pusztai and L. Hajder, "Accurate calibration of LiDAR-camera systems using ordinary boxes," in *IEEE/CVF International Conference* on Computer Vision Workshops (ICCVW), 2017, pp. 394–402.
- [61] A. Napier, P. Corke, and P. Newman, "Cross-calibration of pushbroom 2d lidars and cameras in natural scenes," in *IEEE International Conference on Robotics and Automation (ICRA)*, 2013, pp. 3679–3684.
- [62] C. Yuan, X. Liu, X. Hong, and F. Zhang, "Pixel-level extrinsic self calibration of high resolution lidar and camera in targetless environments," *IEEE Robotics and Automation Letters (RA-L)*, vol. 6, no. 4, pp. 7517– 7524, 2021.
- [63] J. Rehder, P. Beardsley, R. Siegwart, and P. Furgale, "Spatio-temporal laser to visual/inertial calibration with applications to hand-held, large scale scanning," in *IEEE/RSJ International Conference on Intelligent Robots and Systems (IROS)*, 2014, pp. 459–465.

- [64] C. Park, P. Moghadam, S. Kim, S. Sridharan, and C. Fookes, "Spatiotemporal camera-LiDAR calibration: A targetless and structureless approach," *IEEE Robotics and Automation Letters (RA-L)*, vol. 5, no. 2, pp. 1556–1563, 2020.
- [65] C. Ye, H. Pan, and H. Gao, "Keypoint-based LiDAR-camera online calibration with robust geometric network," *IEEE Transactions on Instrumentation and Measurement (TIM)*, vol. 71, pp. 1–11, 2021.
- [66] G. Pandey, J. McBride, S. Savarese, and R. Eustice, "Automatic target-less extrinsic calibration of a 3d lidar and camera by maximizing mutual information," in AAAI Conference on Artificial Intelligence (AAAI), 2012.
- [67] R. Wang, F. P. Ferrie, and J. Macfarlane, "Automatic registration of mobile LiDAR and spherical panoramas," in *IEEE/CVF Conference on Computer Vision and Pattern Recognition Workshops (CVPRW)*, 2012, pp. 33–40.
- [68] N. Schneider, F. Piewak, C. Stiller, and U. Franke, "RegNet: Multimodal sensor registration using deep neural networks," in *IEEE intelligent* vehicles symposium (IV), 2017, pp. 1803–1810.
- [69] G. Iyer, R. K. Ram, J. K. Murthy, and K. M. Krishna, "CalibNet: Geometrically supervised extrinsic calibration using 3d spatial transformer networks," in *IEEE/RSJ International Conference on Intelligent Robots* and Systems (IROS), 2018, pp. 1110–1117.
- [70] X. Lv, B. Wang, Z. Dou, D. Ye, and S. Wang, "LCCNet: LiDAR and camera self-calibration using cost volume network," in *IEEE/CVF Conference on Computer Vision and Pattern Recognition Workshops* (CVPRW), 2021, pp. 2894–2901.
- [71] X. Jing, X. Ding, R. Xiong, H. Deng, and Y. Wang, "DXQ-Net: differentiable lidar-camera extrinsic calibration using quality-aware flow," in *IEEE/RSJ International Conference on Intelligent Robots and Systems* (IROS), 2022, pp. 6235–6241.
- [72] L. F. T. Fu and M. Fallon, "Batch Differentiable Pose Refinement for In-The-wild Camera/LiDAR Extrinsic Calibration," in *Conference on Robot Learning (CoRL)*, 2023.
- [73] Q. Herau, M. Bennehar, A. Moreau, N. Piasco, L. Roldao, D. Tsishkou, C. Migniot, P. Vasseur, and C. Demonceaux, "3dgs-calib: 3d gaussian splatting for multimodal spatiotemporal calibration," in *IEEE/RSJ Inter*national Conference on Intelligent Robots and Systems (IROS), 2024, pp. 8315–8321.
- [74] H. Djeghim, N. Piasco, M. Bennehar, L. Roldão, D. Tsishkou, and D. Sidibé, "Viineus: Volumetric initialization for implicit neural surface reconstruction of urban scenes with limited image overlap," 2025. [Online]. Available: https://arxiv.org/abs/2403.10344
- [75] G. Yan, J. Pi, J. Guo, Z. Luo, M. Dou, N. Deng, Q. Huang, D. Fu, L. Wen, P. Cai, X. Gao, X. Cai, B. Zhang, X. Yang, Y. Bai, H. Zhou, and B. Shi, "Oasim: an open and adaptive simulator based on neural rendering for autonomous driving," 2024.
- [76] E. Olson and M. Kaess, "Evaluating the performance of map optimization algorithms," in RSS Workshop on Good Experimental Methodology in Robotics, vol. 15, 2009, p. 35.
- [77] G. Grisetti, H. Strasdat, K. Konolige, and W. Burgard, "g2o: A general framework for graph optimization," in *IEEE International Conference* on Robotics and Automation (ICRA), vol. 2, 2011, p. 1.
- [78] D. Recasens Lafuente, M. R. Oswald, M. Pollefeys, and J. Civera, "The drunkard's odometry: estimating camera motion in deforming scenes," *Advances in neural information processing systems (NeurIPS)*, vol. 36, pp. 48 877–48 889, 2023.
- [79] R. Martin-Brualla, N. Radwan, M. S. Sajjadi, J. T. Barron, A. Dosovit-skiy, and D. Duckworth, "Nerf in the wild: Neural radiance fields for unconstrained photo collections," in *IEEE/CVF Conference on Computer Vision and Pattern Recognition (CVPR)*, 2021, pp. 7210–7219.
- [80] E. Brachmann, J. Wynn, S. Chen, T. Cavallari, Á. Monszpart, D. Turmukhambetov, and V. A. Prisacariu, "Scene coordinate reconstruction: Posing of image collections via incremental learning of a relocalizer," in *European conference on computer vision (ECCV)*. Springer, 2024, pp. 421–440.
- [81] E. Brachmann, M. Humenberger, C. Rother, and T. Sattler, "On the limits of pseudo ground truth in visual camera re-localisation," in *IEEE/CVF* international conference on computer vision (ICCV), 2021, pp. 6218– 6228.
- [82] M. Tancik, E. Weber, E. Ng, R. Li, B. Yi, T. Wang, A. Kristoffersen, J. Austin, K. Salahi, A. Ahuja et al., "Nerfstudio: A modular framework for neural radiance field development," in ACM SIGGRAPH Conference Proceedings, 2023, pp. 1–12.
- [83] K. Shoemake, "Animating rotation with quaternion curves," in Proceedings of the 12th annual conference on Computer graphics and interactive techniques, 1985, pp. 245–254.

- [84] Q. Ma, D. P. Paudel, A. Chhatkuli, and L. Van Gool, "Continuous pose for monocular cameras in neural implicit representation," in *IEEE/CVF* Conference on Computer Vision and Pattern Recognition (CVPR), 2024, pp. 5291–5301.
- [85] B. Kerbl, G. Kopanas, T. Leimkühler, and G. Drettakis, "3d gaussian splatting for real-time radiance field rendering," *ACM Transactions on Graphics (ToG)*, vol. 42, no. 4, 2023.
- [86] A. Geiger, P. Lenz, C. Stiller, and R. Urtasun, "Vision meets robotics: The kitti dataset," *The International Journal of Robotics Research*, vol. 32, no. 11, pp. 1231–1237, 2013.